Proceedings of the Canadian Society for Mechanical Engineering International Congress
32nd Annual Conference of the Computational Fluid Dynamics Society of Canada
Canadian Society of Rheology Symposium
CSME/CFDSC/CSR 2025
May 25–28, 2025, Montréal, Québec, Canada

CAPILLARY FLOW OF HIGHLY VISCOUS SHEAR-THINNING FLUIDS INTO IRREGULAR MICROCHANNELS

Armin Beitollahi[1], Houshang Alamdari[2], Seyed Mohammad Taghavi[1*]

[1]Department of Chemical Engineering, Université Laval, Québec, QC, Canada, G1V 0A6.
[2]Department of Mining, Metallurgical and Materials Engineering and Aluminium Research Centre - REGAL, Université Laval, Québec, QC, Canada, G1V 0A6.
[*]e-mail: Seyed-Mohammad.Taghavi@gch.ulaval.ca

***Abstract*—This study examines the capillary-driven flow of viscous non-Newtonian shear-thinning fluids in microchannels with axial wall variations, modeled using the power-law rheology. The effects of geometrical irregularities on the temporal trend of fluid impregnation length in the microchannel are analyzed. Results indicate that increasing wall irregularities slows the impregnation process by affecting the effective meniscus contact angle and the capillary driving force. This research provides insight into the mixing process in anode manufacturing for the aluminum production industry, focusing on the impregnation of coal-tar pitch and fine coke particles into large open pores of coarse petroleum coke particles.**

***Keywords-component*—capillary-driven flow; shear-thinning fluids; microchannel**

I. Introduction

Fluid impregnation into capillary channels due to capillary pressure is a common phenomenon in many natural and industrial applications [1]. This mechanism also contributes to anode manufacturing for the aluminum production industry as one of its industrial applications, which involves three stages, including mixing, vibro-compaction, and baking. In the mixing stage, coal-tar pitch and petroleum coke are mixed together; subsequently, the resulting product, referred to as anode paste, is subjected to vibration and compaction, followed by baking in a furnace to yield anode blocks that can be utilized in the Hall-Héroult process to produce aluminum [2]. Materials in the mixing stage consist of coarse and fine coke particles and coal-tar pitch. A coarse coke particle is a porous material, and the mixture of fine coke particles and coal-tar pitch could be treated as a homogenous fluid referred to as the binder matrix. Thus, the binder matrix impregnates coarse coke particles in the mixing stage [3], [4]. In terms of rheology, coal-tar pitch shows a Newtonian behavior in a mixing temperature range of 166 °C to 190 °C, while fine coke particles addition to coal-tar pitch results in a non-Newtonian shear-thinning behavior, which is escalated as fine coke particles percentage increases [2]. Also, coarse coke particles have irregular shapes; thus, it is assumed that an open pore in a coarse coke particle could be represented with a single microchannel with geometrical variations along the axial direction. Therefore, in the present article, the capillary-driven flow of non-Newtonian shear-thinning fluids in irregular capillary channels has been investigated to demonstrate the binder matrix impregnation in coarse coke particles in the mixing stage of anode manufacturing.

Literature on non-Newtonian fluid spontaneous capillary-driven flow, referred to as imbibition, is sparse compared to Newtonian fluids [5]. Previous research works on non-Newtonian shear-thinning fluids' spontaneous imbibition in singular channels have considered different channel shapes, including flow in circular tubes [6]–[11], between parallel walls [12], and channels that are uniformly converging and/or diverging along the axial direction [13], [14]. Moreover, the imbibition of non-Newtonian fluids with viscoelastic behavior has also been examined for capillary-driven flow between parallel walls [15]–[17], and converging and/or diverging channels [18], [19]. Consequently, more research works on non-Newtonian fluids spontaneous imbibition, particularly in irregular channels, is needed [5].

In this research, we examine a highly viscous shear-thinning fluid spontaneous penetration in a microchannel with axial wall variations, which represents the binder matrix impregnation into an open pore of a coarse coke particle in the mixing process of anode manufacturing, with

an analytical model. Walls are considered to vary as sine waves, and the effect of changing geometrical irregularity parameters, including the wall wavelength, amplitude, and phase difference, on the temporal trend of fluid impregnation length until the complete filling of an open pore has been investigated.

II. Methodology

A. Equations

The mass conservation equation for an incompressible flow is written as:

$$\frac{\partial \hat{\rho}}{\partial \hat{t}} + \nabla \cdot (\hat{\rho}\,\hat{U}) = 0, \tag{1}$$

where $\hat{\rho}$, $\hat{t}$, and $\hat{U}$ indicate the fluid density, time, and the flow velocity vector, respectively. Subsequently, the Cauchy momentum equation is written as follows:

$$\hat{\rho}\left(\frac{\partial \hat{U}}{\partial \hat{t}} + \hat{U}\cdot\nabla\hat{U}\right) = -\nabla\hat{p} + \nabla\cdot\hat{\tau}, \tag{2}$$

where $\hat{p}$ and $\hat{\tau}$ denote the pressure field and the shear stress tensor, respectively. $\hat{\tau}$ can be written as follows:

$$\hat{\tau} = \hat{\mu}\,(\nabla\hat{U} + \nabla\hat{U}^{T}), \tag{3}$$

where $\hat{\mu}$ is the fluid viscosity. The fluid flow between the two microchannel walls due to capillary pressure is assumed to be in one direction along the channel centerline. Considering $\hat{s}$ and $\hat{l}$ as the coordinates along the channel centerline and normal to $\hat{s}$, respectively, as shown in Figure 1, several assumptions are made to analyze the flow. These include: the flow is incompressible, quasi one dimensional, in steady state ($\frac{\partial}{\partial \hat{t}} = 0$), fully developed ($\frac{\partial \hat{U}}{\partial \hat{s}} = 0$), and the velocity field consists only of the component in the flow direction ($\hat{U}_{\hat{l}} = 0$). By implementing these assumptions in Equations (1) and (2), the equations of motion could be simplified as follows:

$$0 = -\frac{\partial \hat{p}}{\partial \hat{s}} + \frac{\partial \hat{\tau}_{\hat{s}\hat{l}}}{\partial \hat{l}}. \tag{4}$$

Subsequently, by implementing the assumptions in Equation (3), $\hat{\tau}_{\hat{s}\hat{l}}$, which is equal to $\hat{\tau}_{\hat{l}\hat{s}}$, would be written as follows:

$$\hat{\tau}_{\hat{s}\hat{l}} = \hat{\mu}\frac{\partial \hat{U}_{\hat{s}}}{\partial \hat{l}}, \tag{5}$$

where $\hat{U}_{\hat{s}}$ indicates the flow velocity along the channel centerline ($\hat{s}$). The binder matrix is reported to exhibit shear-thinning behavior, which corresponds to the Ostwald–de Waele relationship [2], also known as the power-law model, expressed as follows:

$$\hat{\mu} = \hat{\mu_0}\,|\hat{\dot{\gamma}}|^{n-1}, \tag{6}$$

where $\hat{\mu}$, $\hat{\mu_0}$, $\hat{\dot{\gamma}}$, and n represent the viscosity, consistency index, shear rate, and the power index respectively, with $n > 1$, $n = 1$, and $n < 1$ corresponding to shear-thickening, Newtonian, and shear-thinning fluids, respectively. Also, $\hat{\dot{\gamma}}$ is written as follows:

$$\hat{\dot{\gamma}} = \frac{\partial \hat{U}_{\hat{s}}}{\partial \hat{l}}. \tag{7}$$

Thus, by implementing Equations (5) to (7) in Equation (4), the momentum equation could be written as follows:

$$0 = -\frac{\partial \hat{p}}{\partial \hat{s}} + \hat{\mu_0}\frac{\partial}{\partial \hat{l}}\left(\frac{\partial \hat{U}_{\hat{s}}}{\partial \hat{l}}\left|\frac{\partial \hat{U}_{\hat{s}}}{\partial \hat{l}}\right|^{n-1}\right). \tag{8}$$

In the context of fluid flow between the channel walls due to an existing pressure gradient, the velocity profile is maximum at the center. It must be zero at the walls to satisfy the no-slip boundary condition. Considering $\hat{l} = 0$ along the channel centerline, $\frac{\partial \hat{U}_{\hat{s}}}{\partial \hat{l}}|_{\hat{l}=\hat{h}/2} < 0$ and $\frac{\partial \hat{U}_{\hat{s}}}{\partial \hat{l}}|_{\hat{l}=-\hat{h}/2} > 0$ where $\hat{h}$ indicates the distance between walls. Since the flow is symmetric, we can proceed with solving Equation (8) over a half domain. Considering the bottom half domain from $\hat{l} = -\hat{h}/2$ to $\hat{l} = 0$, $\frac{\partial \hat{U}_{\hat{s}}}{\partial \hat{l}} > 0$; however, $\hat{l}$ must be replaced with $-|\hat{l}|$ in the solution of Equation (8) to account for the whole domain. Therefore, upon integrating the Equation (8) with respect to $\hat{l}$, the following solution will be obtained:

$$\hat{U}_s = \frac{n}{n+1}\left(\frac{1}{\hat{\mu_0}}\frac{\partial \hat{p}}{\partial \hat{s}}\right)^{\frac{1}{n}}(-|\hat{l}|)^{\frac{n+1}{n}} + C, \tag{9}$$

where C is the integration constant. Considering the no-slip boundary condition on walls ($\hat{U_s}|_{\hat{l}=\pm\hat{h}/2} = 0$), Equation (9) will be rearranged as follows:

$$\hat{U}_{\hat{s}}(\hat{l}) = \frac{n}{n+1}\left(\frac{1}{\hat{\mu_0}}\left|\frac{\partial \hat{p}}{\partial \hat{s}}\right|\right)^{\frac{1}{n}}\left(\frac{\hat{h}}{2}\right)^{\frac{n+1}{n}}\left(1 - \left(\frac{2|\hat{l}|}{\hat{h}}\right)^{\frac{n+1}{n}}\right). \tag{10}$$

Subsequently, average velocity, $\hat{\bar{U}}_{\hat{s}}$, is defined as follows:

$$\hat{\bar{U}}_{\hat{s}}\,\hat{h} = \int_{-\hat{h}/2}^{\hat{h}/2}\hat{U}_{\hat{s}}(\hat{l})d\hat{l}. \tag{11}$$

Upon calculating Equation (11) and implementing the solution in Equation (10), the velocity profile could be written as follows:

$$\hat{U}_{\hat{s}}(\hat{l}) = \hat{\bar{U}}_{\hat{s}}\left(\frac{2n+1}{n+1}\right)\left[1 - \left(\frac{2|\hat{l}|}{\hat{h}}\right)^{\frac{n+1}{n}}\right]. \tag{12}$$

It should be noted this approach of deriving the velocity profile for non-Newtonian fluids conforming to the power-law model has been initially introduced by Bird, Armstrong, and Hassager [20]. Yet, $\hat{h}$ tends to vary along the length for capillary-driven flow in microchannels with wall variations, as shown in Figure 1. Therefore, the average velocity should also vary due to its dependence on the microchannel width; thus, Equation (12) should be modified to account for irregular capillaries written as follows:

$$\hat{U}_{\hat{s}}(\hat{l},\hat{s}) = \hat{\bar{U}}_{\hat{s}}(\hat{s})\left(\frac{2n+1}{n+1}\right)\left[1 - \left(\frac{2|\hat{l}|}{\hat{h}(\hat{s})}\right)^{\frac{n+1}{n}}\right]. \tag{13}$$

In the case of capillary-driven flow of highly viscous fluids, which is the case for the binder matrix impregnation, the effect of inertia is negligible, and this process is also quasi-steady. Therefore, the momentum equation balances pressure and viscous terms as indicated in Equation (2). Considering a differential volume element illustrated with dark blue in Figure 1, the balance of forces, including viscous and pressure terms, could be written as follows:

$$2\hat{\tau}_{\hat{s}\hat{l}}(\hat{s},\hat{h}/2)d\hat{s} - \hat{h}(\hat{s})\frac{\partial\hat{p}}{\partial\hat{s}}d\hat{s} = 0, \tag{14}$$

where $\hat{\tau}_{\hat{s}\hat{l}}(\hat{s},\hat{h}/2)$ is the shear stress on the upper wall, which is identical to the shear stress on the bottom wall ($\hat{\tau}_{\hat{s}\hat{l}}(\hat{s},-\hat{h}/2)$) accounting for the appearance of a coefficient 2 in Equation (14). Upon dividing Equation (14) by $\hat{h}(\hat{s})$ and integrating this equation from the microchannel inlet ($\hat{s}=0$) to the meniscus location ($\hat{s}=\hat{L}$), which is shown in Figure 1, Equation (14) would be written as follows:

$$\underbrace{\int_0^{\hat{L}} \frac{2\hat{\tau}_{\hat{s}\hat{l}}(\hat{s},\hat{h}/2)}{\hat{h}(\hat{s})}d\hat{s}}_{\text{Viscous term}} - \underbrace{\int_0^{\hat{L}} \frac{\partial\hat{p}}{\partial\hat{s}}d\hat{s}}_{\text{Pressure term}} = 0. \tag{15}$$

Subsequently, by implementing Equations (6), (7) and (13) in Equation (5), $\hat{\tau}_{\hat{s}\hat{l}}(\hat{s},\hat{h}/2)$ would be written as follows:

$$\hat{\tau}_{\hat{s}\hat{l}}(\hat{s},\hat{h}/2) = -\hat{\mu}_0\left(\frac{\hat{\bar{U}}_{\hat{s}}(\hat{s})}{\hat{h}(\hat{s})}\left(\frac{4n+2}{n}\right)\right)^n. \tag{16}$$

Thus, by implementing Equation (16) into the viscous term in Equation (15) it could be written as follows:

$$\int_0^{\hat{L}} \frac{2\hat{\tau}_{\hat{s}\hat{l}}(\hat{s},\hat{h}/2)}{\hat{h}(\hat{s})}d\hat{s} = -2\hat{\mu}_0\int_0^{\hat{L}} \frac{\hat{\bar{U}}_{\hat{s}}^{\,n}(\hat{s})}{\hat{h}^n(\hat{s})}\left(\frac{4n+2}{n}\right)^n d\hat{s}. \tag{17}$$

The flow rate at each time remains constant at all sections from the inlet to the meniscus location; therefore, the following correlation could be written:

$$\hat{\bar{U}}_{\hat{s}}(\hat{s})\,\hat{h}(\hat{s}) = \hat{\bar{U}}_{\hat{s}}(\hat{L})\,\hat{h}(\hat{L}), \tag{18}$$

where $\hat{\bar{U}}_{\hat{s}}(\hat{L})$ denotes the average flow velocity at the meniscus location, which is considered the impregnation velocity ($\dot{\hat{L}}$) in this research. Consequently, by substituting Equation (18) in Equation (17) it could be written as:

$$-2\hat{\mu}_0\left(\frac{4n+2}{n}\right)^n \hat{L}^n\hat{h}^n(\hat{L})\int_0^{\hat{L}}\frac{\mathrm{d}\hat{s}}{\hat{h}^{(2n+1)}(\hat{s})} = \int_0^{\hat{L}}\frac{2\hat{\tau}_{\hat{s}\hat{l}}(\hat{s},\hat{h}/2)}{\hat{h}(\hat{s})}\,d\hat{s}. \tag{19}$$

On the other hand, the pressure term in Equation (15) equals to the capillary pressure written as follows:

$$-\int_0^{\hat{L}}\frac{\partial\hat{p}}{\partial\hat{s}}d\hat{s} = \frac{2\hat{\sigma}}{\hat{h}(\hat{L})}\cos\tilde{\theta}, \tag{20}$$

where $\tilde{\theta}$ is the effective contact angle, which is the linear summation of the static contact angle, θ_0, and the wall slope at the location of the meniscus, $tan^{-1}\frac{1}{2}\hat{h}'(\hat{L})$, shown in Figure 1. Also, $\hat{\sigma}$ is the fluid-air surface tension. Eventually, by implementing Equation (19) and Equation (20) in Equation (15), the governing equation of motion for the capillary flow of a highly viscous power-law fluid in an irregular microchannel neglecting inertia and gravity contributions could be written as follows:

$$\hat{L}^n\left[2\hat{\mu}_0\left(\frac{4n+2}{n}\right)^n\hat{h}^n(\hat{L})\int_0^{\hat{L}}\frac{\mathrm{d}\hat{s}}{\hat{h}^{(2n+1)}(\hat{s})}\right] - \frac{2\hat{\sigma}}{\hat{h}(\hat{L})}\cos\tilde{\theta} = 0. \tag{21}$$

Considering $n=1$, which is the case for Newtonian fluids, Equation (17) yields the governing equation of motion presented by Shobeiri and Ponga [21] in the absence of gravity, inertia, and the dynamic contact angle effect.

When the fluid-air interface remains stationary in thermodynamic equilibrium, its contact angle on the wall remains constant, equal to static contact angle, θ_0. On the contrary, as the interface moves, the contact angle on the wall changes with time, known as dynamic contact angle, θ_D, which is complex to analyze. Thus, different mathematical models have been presented in the literature to correlate θ_D to the $\dot{L}$ (interface velocity) and θ_0 [22]–[24]. Moreover, the contact angle modification should be applied on $\tilde{\theta}$ rather than θ_0 for analyzing capillary-driven flow in irregular channels [21]. Here, the molecular kinetic theory (MKT) has been employed to model the dynamic contact angle effect. According to this theory, if the probability of molecular motion in the forward direction is higher than in the backward direction, the interface moves forward, and vice versa. Interface equilibrium occurs when the molecular motion probability in both directions is equal [22]–[24]. Although various versions and interpretations of MKT have been reported in the literature, this research employs the following form of MKT, which is a modified version of the model presented in reference [25], accounting for two-dimensional microchannels, as follows:

$$\cos\tilde{\theta}_0 - \cos\tilde{\theta}_{\mathrm{D}} = \beta\,\frac{\hat{\mu}_0}{\hat{\sigma}}\left(\frac{4n+2}{n}\right)^{n-1}\hat{\dot{L}}^{\,n}\hat{h}^{1-n}(\hat{L}), \tag{22}$$

where $\tilde{\theta}_{\mathrm{i}} = \theta_i + tan^{-1}\frac{1}{2}\hat{h}'(\hat{L})$, and β is a combination of parameters that could be approached as a fitting parameter [25], which is considered 9 in this research. Thus, by implementing Equation (22) in Equation (21), the governing equation of motion could be written as follows:

$$\hat{\dot{L}}^n\left[2\hat{\mu}_0\left(\frac{4n+2}{n}\right)^n\hat{h}^n(\hat{L})\int_0^{\hat{L}}\frac{\mathrm{d}\hat{s}}{\hat{h}^{(2n+1)}(\hat{s})} + \frac{2\beta\,\hat{\mu}_0}{\hat{h}^n(L)}\left(\frac{4n+2}{n}\right)^{n-1}\right] - \frac{2\hat{\sigma}}{\hat{h}(\hat{L})}\cos\tilde{\theta}_0 = 0. \tag{23}$$

Finally, the time-dependent impregnation length, $\hat{L}(\hat{t})$, will be found upon solving Equation (23) numerically using the 4th-order Runge–Kutta method with $\hat{L}(0)=0$.

B. Geometrical considerations

Geometrical features of a microchannel with wavy walls in the shape of a sine wave, including the wall wave length, $\hat{\lambda}$, amplitude, $\hat{A}$, and phase difference, $\hat{\varphi}$, and the channel length, $\hat{L}_{channel}$, and width at the inlet, $\hat{h}(0)$, are illustrated in Figure 1, which demonstrates the binder matrix impregnation in a single large open pore of a coarse petroleum coke particle in the mixing process of anode manufacturing.

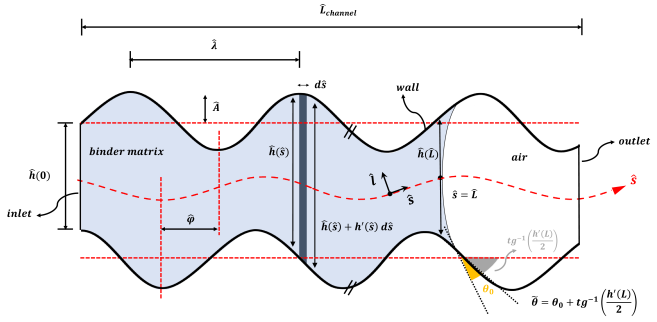

Fig. 1. Geometrical features for a single irregular microchannel with wavy walls representing an open pore in a coarse coke particle subjected to the binder matrix impregnation during mixing.

Coarse coke particles' large open pores are from $300\mu m$ to $500\mu m$ [3]; therefore, $\hat{h}(0)$ is chosen $400\mu m$. Also, the channel length ($\hat{L}_{channel}$) is considered $2400\mu m$. The effect of other parameters' variations on the temporal trend of fluid impregnation, including $\varphi = \hat{\varphi}/\hat{\lambda}$, $A = \hat{A}/\hat{h}(0)$, and $\lambda = \hat{\lambda}//\hat{h}(0)$, are discussed in the Results section.

C. Binder matrix properties

Binder matrix properties at different mixing temperatures and percentages of fine petroleum coke particles have been reported by Mollaabbasi, Hansen, Grande, Taghavi, and Alamdari [2]. Since the mixing temperature is held at 178°C in the anode manufacturing industry, the properties of the binder matrix at this temperature, with a 35% weight percentage of fine particles, which is the maximum value reported in reference [2], have been chosen. These correspond to $\hat{\mu_0} = 18.86\,\mathrm{Pa.s^n}$ with $n = 0.89$. Additionally, $\hat{\sigma}$ is considered to be $21 \times 10^{-3}\,\mathrm{N/m^2}$ [26]. Moreover, the coal-tar pitch contact angle on a compact bed consisting of fine coke particles is reported to be within an approximate range of 50° to 65° after sufficient time [27]; thus, θ_0 is set to 57.5°.

D. Range of parameters

Dimensional and dimensionless input governing parameters are lumped in Table I.

TABLE I
RANGE OF INPUT DIMENSIONAL AND NON-DIMENSIONAL PARAMETERS.

Input dimensional parameters		
Parameter	Name	Range or value
$\hat{h}(0)$	Channel inlet width	$4 \times 10^{-4}\ (m)$
$\hat{L}_{\text{channel}}$	Channel length	$2.4 \times 10^{-3}\ (m)$
$\hat{\sigma}$	Surface tension	$2.1 \times 10^{-2}\ (N/m)$
$\hat{\mu_0}$	Power-law consistency index	$18.86\ (Pa.s^n)$
Input non-dimensional parameters		
Parameter	Name	Range or value
n	Power-law power index	0.89
θ_0	Static contact angle	$57.5\,deg.$
λ	Wall wavelength, $\hat{\lambda}/\hat{h}(0)$	$1-3$
A	Wall amplitude, $\hat{A}/\hat{h}(0)$	$0.05-15$
φ	Wall phase difference, $\hat{\varphi}/\hat{\lambda}$	$0-0.5$
β	MKT fitting parameter	9

III. RESULTS

A. Effect of wall amplitude

The effect of changing wall amplitude on the temporal trend of the impregnation length until an open pore complete filling for $\lambda = 1.5$ and $\varphi = 0$ is shown in Figure 2.

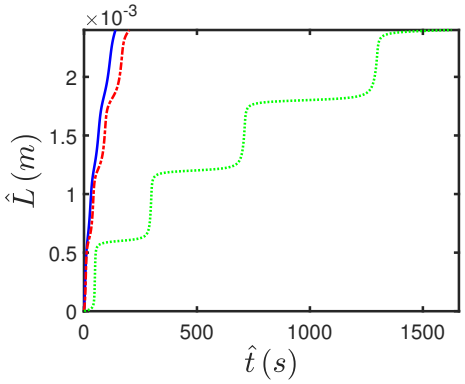

Fig. 2. Effect of changing the wall amplitude in dimensionless form (A) on the temporal trend of meniscus impregnation length for $A = 0.05$ (blue solid line), 0.1 (red dash-dotted line), and 0.15 (green dotted line) with $\lambda = 1.5$ and $\varphi = 0$.

As shown, the binder matrix impregnation slows by increasing A from 0.05 to 0.15 leading to an almost 12 times rise in the complete filling time. This effect is attributed to a steep increase in the wall slope by rising A leading to increasing $\tilde{\theta}$; hence, weakening the capillary driving force. As changes in the wall slope increase, the interface curvature tends to decrease at diverging sections and increase in converging sections within the microchannel. Since the capillary driving force relies on the interface curvature, an increase in the curvature enhances the driving force and vice versa. Thus, by increasing A, fluid impregnation tends to decelerate in diverging sections and accelerate in converging sections resulting in the temporal impregnation length marching toward a horizontal and vertical

line in diverging and converging sections, respectively. This effect is significantly emphasized for $A = 0.15$, while results for the cases with $A = 0.05$ and 0.1 seem to be close. Overall, an open pore's complete filling time rises with an increase in geometrical irregularity in terms of increasing A.

B. Effect of wall wavelength

The effect of changing wall wavelength on the time-dependent trend of the meniscus infiltration length for $A = 0.1$ and $\varphi = 0$ is shown in Figure 3.

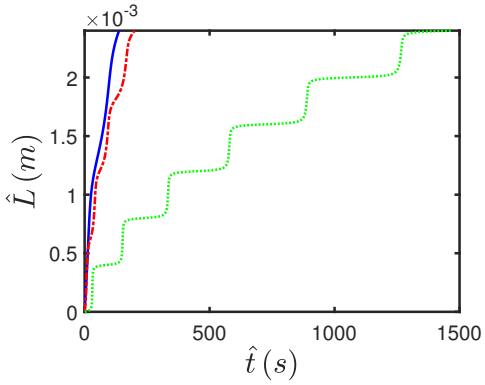

Fig. 3. Effect of changing the wall wavelength in dimensionless form (λ) on meniscus impregnation length versus time for $\lambda = 3$ (blue solid line), 1.5 (red dash-dotted line), and 1 (green dotted line) with $\varphi = 0$ and $A = 0.1$.

As shown, meniscus impregnation prolongs with decreasing λ from 3 to 1, which results in an approximate 11 times increase in microchannel complete filling time. The effect of reducing λ on fluid impregnation length is similar to increasing A as it causes a surge in the wall slope, and it results in slowing down the fluid's infiltration as discussed in the preceding section. Moreover, the number of diverging-converging sections increases with decreasing λ, which culminates in a rise in the number of semi-vertical and semi-horizontal trends in the temporal trend of the impregnation length as shown in Figure 3. These effects become noticeable for cases with a lower λ due to a growth in fluid's deceleration and acceleration in diverging and converging sections, respectively, similar to the impact of increasing A. Overall, an open pore filling time prolongs with a decrease in the wall wavelength, which results in increasing geometrical irregularity.

C. Effect of wall phase difference

The effect of changing wall phase difference on the temporal trend of the infiltration length for $A = 0.1$ and $\lambda = 1.5$ is shown in Figure 4.

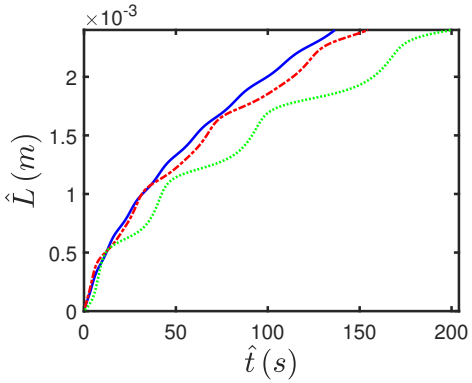

Fig. 4. Effect of changing the walls' phase difference in dimensionless form (φ) on the time-dependent trend of meniscus impregnation length for $\varphi = 0$ (blue solid line), 0.25 (red dash-dotted line), and 0.5 (green dotted line) with $\lambda = 1.5$ and $A = 0.1$.

By increasing φ from 0 (parallel wall arrangement) to 0.5 (symmetric wall arrangement), the time of complete microchannel filling 1.5 times increases as illustrated in Figure 4. This effect is due to the influence of wall phase difference on the meniscus effective contact angle. As φ increases, the microchannel width variations tend to rise, which results in growing changes in the spatial derivative of the microchannel width at the meniscus location, $\hat{h}'(\hat{L})$. Therefore, changes in the effective contact angle are likely to increase, which culminates in weakening the capillary driving force and elevating the impregnation time of the meniscus within the microchannel. Yet, the impact of increasing φ on prolonging the impregnation time is less influential compared to rising A and decreasing λ.

IV. CONCLUSION

This research highlights the influence of geometrical parameters on the temporal trend of shear-thinning fluids' impregnation length in microchannels with wall irregularities, with the capillary pressure being the driving force. The main application of this research is analyzing the mixing stage in anode manufacturing for the aluminum production industry, where the mixture of coal-tar pitch and fine coke particles as a shear-thinning fluid impregnates open pores of coarse coke particles, which is modeled with a single microchannel with wall variations. An analytical method has been proposed for analyzing the capillary-driven flow of fluids conforming to the power-law rheology model, particularly shear-thinning fluids, in irregular microchannels. For the parametric study, the microchannel walls were considered two separate sine waves, and the effects of geometrical features, including the walls' wavelength, amplitude, and phase difference, were investigated. The results indicated that increasing wall amplitude or decreasing wall wavelength significantly escalates impregnation time due to changes in wall slope, effective contact angle, and the driving force. In addition, increasing the walls' phase difference from a

parallel to a symmetric wall arrangement modestly increases filling time due to similar reasons; however, its impact on raising impregnation time is less significant than the other two parameters. This study advances the understanding of shear-thinning fluids' capillary-driven flow in irregular capillaries. Also, it provides a foundation for future work on developing extended models accounting for the mixing process in anode manufacturing.

REFERENCES

[1] J. Cai, T. Jin, J. Kou, S. Zou, J. Xiao, and Q. Meng, "Lucas–Washburn Equation-Based Modeling of Capillary-Driven Flow in Porous Systems," Langmuir, vol. 37, no. 5, pp. 1623–1636, Jan. 2021.

[2] R. Mollaabbasi, L. J. Hansen, T. Grande, S. M. Taghavi, and H. Alamdari, "Effect of fine coke particles on rheological properties of the binder matrix of carbon anodes in aluminium production process," The Canadian Journal of Chemical Engineering, vol. 100, no. S1, Mar. 2021.

[3] K. Azari, H. Alamdari, G. Aryanpour, D. Picard, M. Fafard, and A. Adams, "Mixing variables for prebaked anodes used in aluminum production," Powder Technology, vol. 235, pp. 341–348, Feb. 2013.

[4] K. Azari, H. Alamdari, D. Ziegler, and M. Fafard, "Influence of coke particle characteristics on the compaction properties of carbon paste material," Powder Technology, vol. 257, pp. 132–140, May 2014.

[5] J. Cai, Y. Chen, Y. Liu, S. Li, and C. Sun, "Capillary imbibition and flow of wetting liquid in irregular capillaries: A 100-year review," Advances in Colloid and Interface Science, vol. 304, pp. 102654–102654, Jun. 2022.

[6] R. M. Digilov, "Capillary Rise of a Non-Newtonian Power Law Liquid: Impact of the Fluid Rheology and Dynamic Contact Angle," Langmuir, vol. 24, no. 23, pp. 13663–13667, Nov. 2008.

[7] S. Cito, Y. C. Ahn, J. Pallares, R. M. Duarte, Z. Chen, M. Madou, and I. Katakis, "Visualization and measurement of capillary-driven blood flow using spectral domain optical coherence tomography," vol. 13, no. 2, pp. 227–237, Feb. 2012.

[8] H. Kim, J.-H. Lim, K. Lee, and S. Q. Choi, "Direct Measurement of Contact Angle Change in Capillary Rise," Langmuir, vol. 36, no. 48, pp. 14597–14606, Nov. 2020.

[9] F. Shan, Z. Chai, and B. Shi, "A theoretical study on the capillary rise of non-Newtonian power-law fluids," Applied Mathematical Modelling, vol. 81, pp. 768–786, May 2020.

[10] C. Steinik, D. Picchi, G. Lavalle, and P. Poesio, "Capillary imbibition of shear-thinning fluids: From Lucas-Washburn to oscillatory regimes," Physical Review Fluids, vol. 9, no. 2, Feb. 2024.

[11] X. Wang, Z. Yuan, F. Chen, X. Yao, F. Yu, and S. Wang, "Forced Wetting of Shear-Thinning Fluids in Confined Capillaries," Langmuir, Sep. 2024.

[12] F. Shan, H. Du, Z. Chai, and B. Shi, "Lattice Boltzmann modeling of the capillary rise of non-Newtonian power-law fluids," International Journal for Numerical Methods in Fluids, vol. 94, no. 3, pp. 251–271, Sep. 2021.

[13] C. L. A. Berli and R. Urteaga, "Asymmetric capillary filling of non-Newtonian power law fluids," Microfluidics and Nanofluidics, vol. 17, no. 6, pp. 1079–1084, Mar. 2014.

[14] S. Kalia, Y. Rawat, P. K. Mondal, and S. Wongwises, "Capillary imbibition of inelastic non-Newtonian fluids in an asymmetric flow assay," European Journal of Mechanics - B/Fluids, vol. 101, pp. 22–29, May 2023.

[15] A. Bandopadhyay, U. Ghosh, and S. Chakraborty, "Capillary filling dynamics of viscoelastic fluids," Physical Review E, vol. 89, no. 5, May 2014.

[16] H. S. Gaikwad, A. Roy, and P. K. Mondal, "Autonomous filling of a viscoelastic fluid in a microfluidic channel: Effect of streaming potential," Journal of Non-Newtonian Fluid Mechanics, vol. 282, p. 104317, Aug. 2020.

[17] A. Roy and P. Dhar, "Micro-imbibition electro-magneto-hydrodynamics of viscoelastic fluids with interactive streaming potential," Journal of Non-Newtonian Fluid Mechanics, vol. 310, p. 104936, Dec. 2022.

[18] Y. Rawat, S. Kalia, and P. K. Mondal, "Quantitative model for predicting the imbibition dynamics of viscoelastic fluids in nonuniform microfluidic assays," Physical review. E, vol. 104, no. 5, Nov. 2021.

[19] A. Roy and P. Dhar, "Capillary Orientation and Morphology Dictated Oscillatory Electro-magneto-imbibition of Viscoelastic Electrolytes," Langmuir, vol. 40, no. 45, pp. 23788–23805, Oct. 2024.

[20] R. B. Bird, R. C. Armstrong, and O. Hassager, "Dynamics of Polymeric Liquids," 2nd ed., vol. 1, John Wiley & Sons, New York, 1987.

[21] A. Shobeiri and M. Ponga, "A visco-inertial formulation for capillarity in irregular channels and tubes," Physics of Fluids, vol. 33, no. 11, Nov. 2021.

[22] G. Lu, X.-D. Wang, and Y.-Y. Duan, "A Critical Review of Dynamic Wetting by Complex Fluids: From Newtonian Fluids to Non-Newtonian Fluids and Nanofluids," Advances in Colloid and Interface Science, vol. 236, pp. 43–62, Oct. 2016.

[23] A. M. Karim and W. J. Suszynski, "Physics of Dynamic Contact Line: Hydrodynamics Theory versus Molecular Kinetic Theory," Fluids, vol. 7, no. 10, pp. 318–318, Sep. 2022.

[24] Y. Zhang, M. Guo, D. Seveno, and J. D. Coninck, "Dynamic wetting of various liquids: Theoretical models, experiments, simulations and applications," Advances in Colloid and Interface Science, vol. 313, pp. 102861–102861, Mar. 2023.

[25] H. Kim, J.-H. Lim, K. Lee, and S. Q. Choi, "Direct Measurement of Contact Angle Change in Capillary Rise," Langmuir, vol. 36, no. 48, pp. 14597–14606, Nov. 2020.

[26] Y. Lu, A. Hussein, D. Li, X. Huang, R. Mollaabbasi, D. Picard, T. Ollevier, and H. Alamdari, "Properties of Bio-pitch and Its Wettability on Coke," ACS Sustainable Chemistry & Engineering, vol. 8, no. 40, pp. 15366–15374, Sep. 2020.

[27] A. Sarkar, D. Kocaefe, Y. Kocaefe, D. Sarkar, D. Bhattacharyay, B. Morais, and J. Chabot, "Coke–pitch interactions during anode preparation," Fuel, vol. 117, pp. 598–607, Jan. 2014.